

# Excellent Bifunctional Oxygen Evolution and Reduction Electrocatalysts $(5A_{1/5})\text{Co}_2\text{O}_4$ and Their Tunability

Published as part of ACS Materials Au virtual special issue "2023 Rising Stars".

Xin Wang, Harish Singh, Manashi Nath, Kurt Lagemann, and Katharine Page\*



Cite This: *ACS Mater. Au* 2024, 4, 274–285



Read Online

ACCESS |

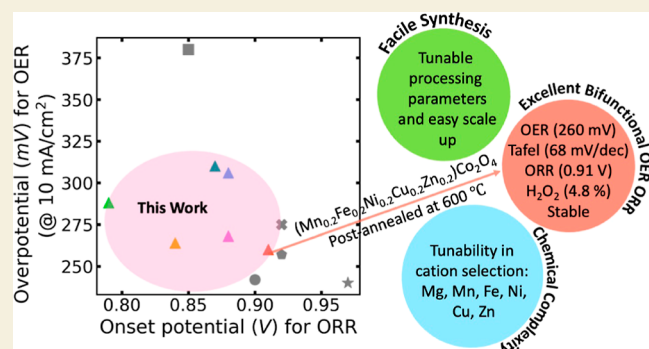
Metrics & More

Article Recommendations

Supporting Information

**ABSTRACT:** Hastening the progress of rechargeable metal–air batteries and hydrogen fuel cells necessitates the advancement of economically feasible, earth-abundant, inexpensive, and efficient electrocatalysts facilitating both the oxygen evolution reaction (OER) and oxygen reduction reaction (ORR). Herein, a recently reported family of nano  $(5A_{1/5})\text{Co}_2\text{O}_4$  ( $A =$  combinations of transition metals, Mg, Mn, Fe, Ni, Cu, and Zn) compositionally complex oxides (CCOs) [Wang et al., *Chemistry of Materials*, 2023, 35 (17), 7283–7291.] are studied as bifunctional OER and ORR electrocatalysts. Among the different low-temperature soft-templating samples, those subjected to 600 °C postannealing heat treatment exhibit superior performance in alkaline media. One specific composition  $(\text{Mn}_{0.2}\text{Fe}_{0.2}\text{Ni}_{0.2}\text{Cu}_{0.2}\text{Zn}_{0.2})\text{Co}_2\text{O}_4$  exhibited an exceptional overpotential (260 mV at  $10 \text{ mA cm}^{-2}$ ) for the OER, a favorable Tafel slope of  $68 \text{ mV dec}^{-1}$ , excellent onset potential (0.9 V) for the ORR, and lower than 6%  $\text{H}_2\text{O}_2$  yields over a potential range of 0.2 to 0.8 V vs the reversible hydrogen electrode. Furthermore, this catalyst displayed stability over a 22 h chronoamperometry measurement, as confirmed by X-ray photoelectron spectroscopy analysis. Considering the outstanding performance, the low cost and scalability of the synthesis method, and the demonstrated tunability through chemical substitutions and processing variables, CCO  $\text{ACo}_2\text{O}_4$  spinel oxides are highly promising candidates for future sustainable electrocatalytic applications.

**KEYWORDS:** bifunctional electrocatalyst, OER, ORR, solid solution, low temperature soft-template, compositionally complex oxide, cobaltite, high entropy oxide



## INTRODUCTION

Water splitting to produce hydrogen via the electrolysis pathway is considered a promising direction toward carbon-free energy production, especially considering the potential utilization of widely distributed renewable (wind, solar, and geothermal) and nuclear energy sources.<sup>1</sup> A key research challenge lies in improving the energy efficiency for converting electricity to hydrogen over a wide range of operating conditions.<sup>2</sup> With this regard, designing and developing economically feasible, earth-abundant, inexpensive, efficient electrocatalysts for the oxygen evolution reaction (OER) is a critical research factor.<sup>3–5</sup> Even further, searching for electrocatalysts which can boost both the OER and the oxygen reduction reaction (ORR) simultaneously is crucial for deploying hydrogen production in a useable form, e.g., fuel cells,<sup>3</sup> metal–air batteries.<sup>6</sup>

Efficiently developing bifunctional electrocatalysts for the OER and ORR presents two major challenges. Traditional electrocatalyst research primarily focuses on noble metal (Pt, Ir, Ru, etc.) incorporation, inappropriate for large-scale

deployment due to low abundance and high cost.<sup>7</sup> In addition, the best catalysts for OER activity may not excel in ORR and vice versa.<sup>6</sup> One promising avenue of research focuses on low cost transition-metal-based materials, among which cobalt-based spinel-type oxides are particularly promising as bifunctional electrocatalysts.<sup>8,9</sup>

Currently, a number of Co-based spinel-type oxides, including binary oxides such as  $\text{Co}_3\text{O}_4$  as well as related ternary oxides with the formula  $\text{ACo}_2\text{O}_4$  ( $A = \text{Mn, Ni, Cu, Fe, Zn, etc.}$ ), have shown promise as non-noble metal bifunctional catalysts. As summarized by Zhao et al. in their review paper,<sup>8</sup> several strategies are commonly employed to enhance OER and ORR properties in the family of spinels, including

**Received:** October 18, 2023

**Revised:** December 22, 2023

**Accepted:** December 27, 2023

**Published:** January 19, 2024



morphology optimization,<sup>10–19</sup> defect tuning,<sup>20,21</sup> composition engineering (active noble metal substitution<sup>22,23</sup> and complex multimetal synergistic effects<sup>7,24–27</sup>), structure/phase regulating,<sup>2,8</sup> and utilization of conductive substrates.<sup>11,26,27,29–38,38–40,40–51</sup> By implementation of these established and emerging techniques, the performance of electrocatalysts for both the OER and the ORR can be significantly improved. A key figure of merit for assessing OER catalysts is a reduced overpotential value for overcoming the kinetic barrier (thermodynamic potential, 1.23 V) at a current density of 10 mA cm<sup>-2</sup>.<sup>52</sup> For reference, the best reported OER noble-metal catalysts have overpotentials close to 200 mV.<sup>53</sup> Furthermore, the proximity of the onset potential to 1.0 V is a critical performance indicator for the ORR. The best ORR catalysts, Pt-based materials, exhibit an ORR onset potential just below 1.0 V<sup>54–56</sup> and maintain a yield of H<sub>2</sub>O<sub>2</sub> below 5% over a potential range of 0.2 to 0.7 V vs reversible hydrogen electrode (RHE).<sup>49</sup>

Figure 1 presents extracted values of the promising ORR onset potential values (in V) and low OER overpotential

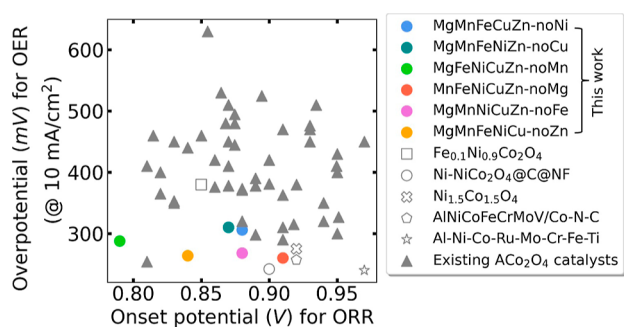


**Figure 1.** Overpotential (measured at 10 mA cm<sup>-2</sup>) for the OER versus onset potential for the ORR for the best-performing (5A<sub>1/5</sub>)Co<sub>2</sub>O<sub>4</sub> spinel CCOs in this work (solid colored circles) compared to existing ACo<sub>2</sub>O<sub>4</sub>-based electrocatalysts from references cited<sup>7,8,10,11–51</sup> (solid gray triangles). Several notable benchmarks are highlighted with hollow gray markers.<sup>19,22,24,26,49</sup> See the text for further details.

values (in mV) from the spinel oxide literature mentioned above (solid gray triangles). Their corresponding substrate and drop-cast mass (mass loading) for OER and ORR studies are summarized in Table S1. It should be noted here that a low overpotential for the OER and a higher onset potential for the ORR are more desirable, as explained above. Hence, more efficient catalysts are expected to occupy the bottom region of this plot and toward the right. Among these catalysts, the complex nitrogen-doped “nanonetwork” assembled from porous and defective NiCo<sub>2</sub>O<sub>4</sub>@C nanowires grown on nickel foam (“N–NiCo<sub>2</sub>O<sub>4</sub>@C@NF”, represented by a hollow gray circle in Figure 1) stands out with its significantly low OER overpotential of 242 mV and relatively high ORR onset potential (0.90 V vs RHE).<sup>49</sup> “Ni<sub>1.5</sub>Co<sub>1.5</sub>O<sub>4</sub>”<sup>19</sup> (represented by a hollow gray “X” in Figure 1), an atomically thin nickel-doped spinel cobalt oxide, exhibits bifunctional catalytic performances with the overpotential of 275 mV for the OER and the onset potential of 0.92 V for the ORR. A seven-component “high entropy oxide” (HEO), “AlNiCoFeCrMoV” integrated with so-called “Co–N–C” (gray hollow pentagon in Figure 1) achieves a highly bifunctional HEO/Co–N–C nanocomposite electrocatalyst, with an overpotential of 257 mV for the OER and an onset potential of 0.92 V for the ORR. These values are

comparable to those of precious metal containing catalysts. One eight-component spinel HEO, “Al–Ni–Co–Ru–Mo–Cr–Fe–Ti”, represented by a hollow gray star in Figure 1 also stands out as a promising bifunctional catalyst (overpotential of 240 mV for the OER and onset potential of 0.97 mV for the ORR), but it notably includes the precious noble metal, Ru.<sup>22</sup>

The strategy of compositional complexity in the cobalt spinel oxide system presents an alternative approach to complicated synthesis and processing routes and precious metal incorporation for bifunctional electrocatalysts, such as the OER and ORR electrocatalysts. HEOs (commonly referred to as single-phase oxides where five or more metal cations occupy a specific crystallographic lattice site in a random manner with configurational entropy equal to or higher than 1.5R per mole of metals/cations, where R represents the universal gas constant) and related compositionally complex oxide (CCO, encompassing medium-entropy and nonequimolar composition oxides) phases offer a number of potential advantages attractive to improved designs for the activity, structural stability, and tunability of electrocatalysts. The sluggish diffusion kinetics associated with decreased cation mobilities reported in a number of CCOs to date<sup>57–59</sup> may lead to slower particle coarsening relative to simpler phases. The increased configurational entropy in CCO/HEO/entropy-stabilized oxide (ESO) phases may offer intrinsic phase stability at high temperatures. Perhaps the most beneficial effect predicted to offer advantages for catalysis is the so-called “cocktail effect”, whereby the catalytic activity of mixed metal cations enriches the type and/or strength of orbital hybridization relative to individual (or less complex) active cation sites. This phenomenon is already well explored in complex oxides, for example, in the enhanced activity reported for M<sub>0.1</sub>Ni<sub>0.9</sub>Co<sub>2</sub>O<sub>4</sub> (M = Mn, Fe, Zn, and Cu) spinels<sup>24</sup> (Fe<sub>0.1</sub>Ni<sub>0.9</sub>Co<sub>2</sub>O<sub>4</sub> is represented by a hollow gray square in Figure 1), cerium-doped CoMn<sub>2</sub>O<sub>4</sub> (Ce–CMO–X) spinels,<sup>23</sup> La<sub>1.5</sub>Sr<sub>0.5</sub>NiMn<sub>0.5</sub>Ru<sub>0.5</sub>O<sub>6</sub> double perovskite,<sup>60</sup> and others described in a number of reviews.<sup>6,9,61</sup> Nonetheless, few bifunctional HEO or CCO catalysts have been studied to date.

We recently reported on a low-temperature soft templating (LTST) reaction route for a wide number of (nA<sub>1/n</sub>)Co<sub>2</sub>O<sub>4</sub> spinel oxides.<sup>62</sup> Figure 2a displays the spinel oxide structure with an inverse cation site model assumed (in the inverse spinel structure, the red tetrahedral cation sites are completely occupied by Co atoms, while blue octahedral cation sites are occupied by 50% Co and 50% A atoms). The chemical compositions, spinel structure, and morphology features make the phases clear candidates for bifunctional electrocatalysts. In this work, we explore the OER and ORR electrocatalytic activity of a family of nano (5A<sub>1/5</sub>)Co<sub>2</sub>O<sub>4</sub> spinel oxides where A contains five equimolar component combinations of the elements Mg, Mn, Fe, Ni, Cu, and Zn. Compared to the existing literature on cobaltites as bifunctional OER and ORR electrocatalysts, the LTST-prepared electrocatalysts in this work postannealed at 600 °C (solid colored circles displayed in Figure 1) demonstrate significantly promising bifunctional OER and ORR performances. Furthermore, catalytic trends for the OER and ORR are demonstrated to be tunable through postprocessing and specific cation selection, indicating a promising design strategy for optimizing new bifunctional catalysts.

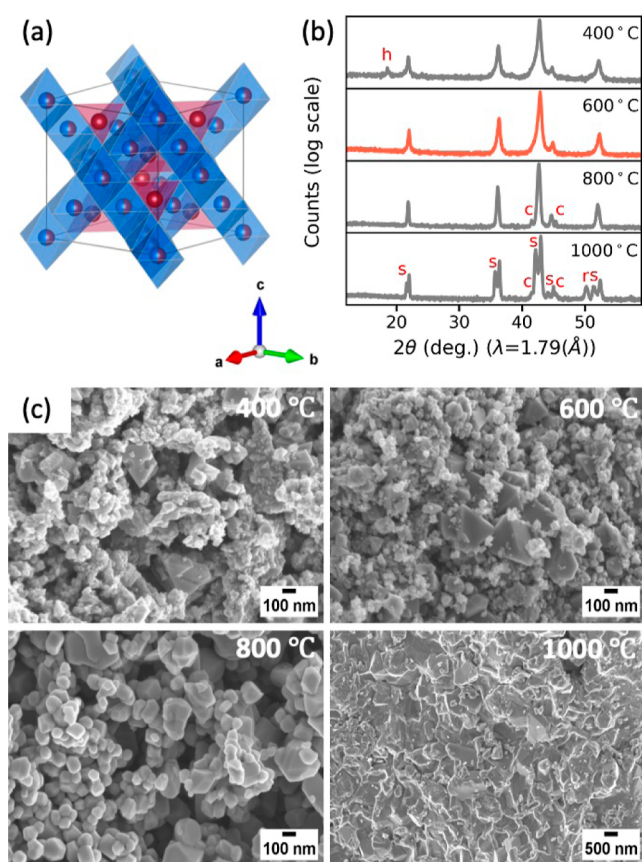


**Figure 2.** (a) Cubic spinel oxide unit cell model with an inverse structure assumed. The red tetrahedral cation sites are completely occupied by Co atoms, while blue octahedral cation sites are occupied by 50% Co and 50% A atoms. Oxygen atoms decorating the corners of the shaded polyhedra are omitted for clarity. (b) XRD patterns of the MnFeNiCuZn–noMg cobaltite series, including the as-prepared sample (400 °C), and samples postannealed at 600, 800, and 1000 °C. Impurities are coded:  $\text{CoCl}_2 \cdot 2\text{H}_2\text{O}$  (“h”); tenorite  $\text{CuO}$  (“c”); rock salt (“r”); and secondary spinel (“s”). (c) Corresponding SEM images for samples in (b).

## EXPERIMENTAL SECTION

### Material Synthesis

The synthesis and phase stability of a large family of  $(n\text{A}_{1/n})\text{Co}_2\text{O}_4$  ( $n = 1$  to 7) spinel nanostructures were recently reported using a LTST reaction route.<sup>62</sup> The structuring agent, Pluronic P123 (3.2 g), was dissolved in 20 mL of ethyl alcohol. Next, 0.5 mL of hydrochloric acid (HCl) was added to the solution and stirred using a magnetic stir bar until the Pluronic P123 was completely dissolved. Then, the desired stoichiometric amounts [1 g  $(n\text{A}_{1/n})\text{Co}_2\text{O}_4$  as the target] of inorganic nitrate/chloride hydrate precursor solutions in wt % of metal were added into the solution. The entire mixed solution was stirred for 30 min using a magnetic stirrer. Subsequently, the mixed solution was transferred to a Petri dish and placed under a fume hood for 24 h to allow for evaporation, resulting in the formation of a wet gel. Once the evaporation was complete, the gel was transferred to a furnace and subjected to calcination at 400 °C for a duration of 5 h. Finally, postannealing treatments were conducted at temperatures of 600, 800, or 1000 °C for 5 h. For samples in the present work,  $n = 5$  refers to an equiatomic combination of five transition-metal cations on the A-site. Sample compositions studied are listed in Table 1, along with an indication of phase purity trends. Representative X-ray diffraction (XRD) data and scanning electron microscopy (SEM) images are shown in Figure 2b,c. XRD patterns of all samples involved in this work can be viewed in our previous work.<sup>62</sup>

**Table 1. Target Compositions with Formula  $(5\text{A}_{1/5})\text{Co}_2\text{O}_4$  Involved in This Work<sup>a</sup>**

name	400 °C	600 °C	800 °C	1000 °C
MgMnFeCuZn–noNi	✓	✓	r	r + s
MgMnFeNiZn–noCu	✓	✓	r	r + s
MgFeNiCuZn–noMn	c + r	c + r	c + r	c + r
MnFeNiCuZn–noMg	h	✓	c	c + r + s
MgMnNiCuZn–noFe	r	r	r	r + s
MgMnFeNiCu–noZn	✓	✓	r	r + s

<sup>a</sup>Samples are obtained after calcination at 400 °C and following postannealing heat treatment at 600, 800, and 1000 °C. Conditions resulting in X-ray pure phases are labeled with check marks, and conditions resulting in phase mixtures are labeled with impurity abbreviations. Impurities are coded:  $\text{CoCl}_2 \cdot 2\text{H}_2\text{O}$  (“h”); tenorite  $\text{CuO}$  (“c”); rock salt (“r”); and secondary spinel (“s”).

We have incorporated different combinations of five equiatomic A elements (with Mg, Mn, Fe, Ni, Cu, and Zn as choices) in each nanocatalyst. The first five elements listed in the sample names denote the five cations incorporated, while the term “noX” indicates the absence of a specific element X in that composition.<sup>62</sup>

### Structure and Morphology Characterization

**X-ray Diffraction.** X-ray Diffraction (XRD) data were measured with a PANalytical Empyrean diffractometer equipped with a  $\text{Co K}\alpha$  source. The XRD patterns were measured between 10 and 90°  $2\theta$  with a step size of 0.026°. The use of  $\text{Co K}\alpha$  radiation was found to be key in uncovering minor impurity phases (the X-ray fluorescence for these samples with  $\text{Cu K}\alpha$  sources masked the presence of minor impurity phases). Rietveld refinements were carried out with the TOPAS-V7 program<sup>63</sup> utilizing a “continuous lattice” model<sup>62</sup> to capture nanoscale inhomogeneity. The cation site inversion parameter (the fraction of A-site ions occupying the octahedral sites,  $\gamma^{27,62}$ ) and crystalline domain size (CS) were also refined.

**Scanning Electron Microscopy/Energy-Dispersive Spectroscopy.** Specimens for Scanning electron microscopy (SEM) and energy-dispersive spectroscopy (EDS) were prepared by gently dispersing the finely ground powders onto standard carbon tape, ensuring optimal sample distribution. The morphologies of the specimens were then characterized using a Zeiss Auriga high-resolution SEM. Elemental analysis was carried out with a Zeiss EVO SEM.

**X-ray Photoelectron Spectroscopy.** X-ray photoelectron spectroscopy (XPS) was conducted with an Al X-ray source on a KRATOS AXIS 165 spectrometer to investigate the surface chemical composition and the valence states of the elements involved before and after the OER stability studies. The acquisition of all XPS data was carried out without any sputtering to accurately examine the surface chemistry.

### Electrochemical Characterization

**Electrode Preparation.** To prepare the homogeneous catalyst ink for analyzing the OER and ORR activity of catalysts, 4 mg of the catalyst was dispersed in 300  $\mu\text{L}$  of ethanol and mixed with Nafion (0.8  $\mu\text{L}$ , 5 wt %). For the OER measurements, the ink required an additional step of 1 h ultrasonication to ensure its homogeneity. Subsequently, 100  $\mu\text{L}$  of the homogenized ink was dropped onto carbon cloth with a geometric area of 0.283  $\text{cm}^2$ . For ORR measurements, the glassy carbon (GC) electrode was polished using 1 and 0.05  $\mu\text{m}$  alumina powder and then sonicated first in isopropanol and then in distilled water. Next, 20  $\mu\text{L}$  of the catalyst ink was drop cast onto the GC working electrode with a geometric area of 0.196  $\text{cm}^2$ . Finally, the electrode was dried under ambient conditions.

**Water Splitting and ORR Measurements.** An IviumStat potentiostat was used for investigating the bifunctional OER and ORR electrocatalytic performances of  $\text{CCO} (5\text{A}_{1/5})\text{Co}_2\text{O}_4$  electrodes. The setup of electrochemical measurements is a three-electrode cell system. The graphite rod is the counter electrode, and the  $\text{Ag}/\text{AgCl}$

(KCl-saturated) is the reference electrode. The 5 mm diameter rotating ring disk electrode (RRDE) is the working electrode for the ORR [in O<sub>2</sub>-saturated 1 M KOH at different rotational rates between 400 and 2000 rpm (10 mV s<sup>-1</sup>)] while catalyst-loaded carbon cloth is the working electrode for the OER (in N<sub>2</sub>-saturated 1 M KOH).

**Tafel Plot.** Tafel slopes of the 600 °C series were calculated by polarization curve fitting to examine the OER performance. The Tafel equation is given below

$$\epsilon = \alpha + \frac{2.3RT}{\alpha nF} \log j \quad (1)$$

where  $\alpha$  is the charge-transfer coefficient,  $n$  is the number of electrons involved in the reaction,  $F$  is the Faraday constant, and other symbols have their usual meanings. The Tafel equation illustrates the dependency of the overpotential  $\epsilon$  on the current density  $j$ . The Tafel slope is given by  $2.3RT/\alpha nF$ .

**Electrochemically Active Surface Area.** The electrochemically active surface area (ECSA) was obtained according to the equation

$$\text{ECSA} = \frac{C_{\text{DL}}}{C_s} \quad (2)$$

where  $C_{\text{DL}}$  is the double-layer capacitance and  $C_s$  is the specific capacitance (0.04 mF cm<sup>-2</sup>, taken from similar catalysts<sup>64</sup>). An average of the absolute values of the cathodic and anodic slopes is calculated to obtain the value of  $C_{\text{DL}}$ . Roughness factor (RF) is another important factor which relates to the surface roughness. It can be defined as ECSA/0.283, where 0.283 cm<sup>2</sup> is the geometric electrode area used for the OER.

## RESULTS AND DISCUSSION

### Bifunctional OER and ORR Electrocatalysts

A screening of the OER performance across the MgMnFeCuZn–noNi, MgMnFeNiZn–noCu, MgFeNiCuZn–noMn, MnFeNiCuZn–noMg, MgMnNiCuZn–noFe, and MgMnFeNiCu–noZn series revealed that the samples treated at different processing temperatures (400, 600, 800, and 1000 °C) exhibit varying overpotential for the OER. Representative overpotential results for the samples involved are presented in Figure S1a. The series of 600 °C processed samples present superior catalytic activity compared to the 400, 800, and 1000 °C sample series. The trend in overpotential values observed is 600 °C < 1000 °C < 800 °C < 400 °C for nearly all compositions (except MgMnFeNiZn–noCu, for which the overpotential of the 400 °C sample  $\approx$  that of the 800 °C sample). In our pursuit of developing a high-performance bifunctional catalyst, we have conducted ORR with the best OER set (the 600 °C series) in this study. To assess their electrokinetic activity, we employed a RRDE setup.

A selection of electrocatalytic data for the sample series is presented in Figure 3, with key values summarized in Table 2. The OER electrocatalytic activity of the 600 °C series were evaluated using linear sweep voltammetry (LSV) measurements, as illustrated in Figure 3a. The extracted overpotential values at 10 mA cm<sup>-2</sup> are those presented as colored symbols in Figure 1, demonstrating that they are among the lowest recorded OER overpotential values for cobaltite-based electrocatalysts in the literature. For samples studied here, the MnFeNiCuZn–noMg-600 °C sample exhibits the highest OER catalytic activity, with an overpotential of approximately 260 mV. This falls within the “ideal” range (200–300 mV at 10 mA cm<sup>-2</sup>) defined by Tahir et al. in their review paper.<sup>53</sup> Additionally, MnFeNiCuZn–noMg-600 °C exhibits a high current density (exceeding 150 mA cm<sup>-2</sup>), indicating favorable conductivity. The corresponding Tafel slopes extracted from

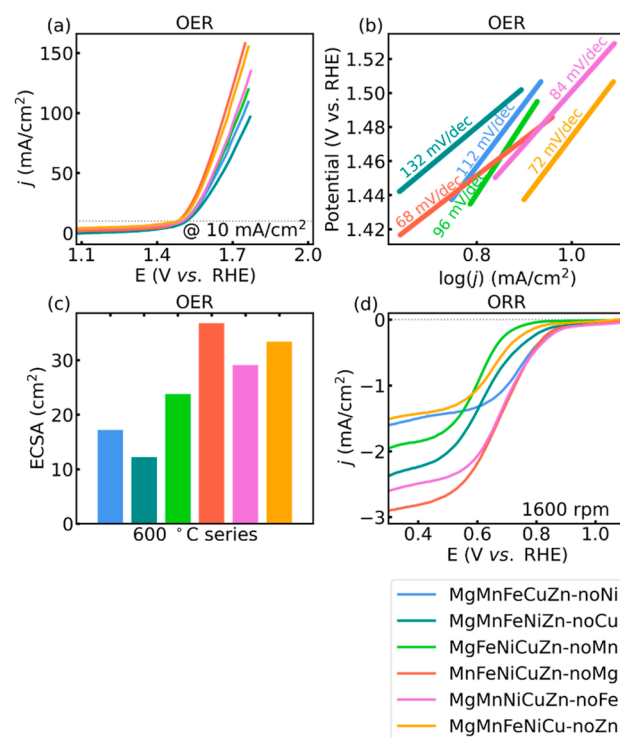


**Figure 3.** (a) OER LSV polarization curves, (b) OER Tafel plots, (c) OER ECSA, and (d) ORR LSV polarization curves at a rotating speed of 1600 rpm for the 600 °C sample series.

OER electrocatalytic activity are displayed in Figure 3b. The Tafel slope values indicate that MnFeNiCuZn–noMg-600 °C has the lowest Tafel slope of 68 mV dec<sup>-1</sup>, outperforming N–NiCo<sub>2</sub>O<sub>4</sub>@C@NF (86 mV dec<sup>-1</sup>)<sup>49</sup> and approaching the performance of Al–Ni–Co–Ru–Mo–Cr–Fe–Ti (51.3 mV dec<sup>-1</sup>).<sup>22</sup> The reaction kinetics are enhanced when the Tafel slope is smaller, leading to a higher current density and subsequently increased oxygen generation. The low Tafel slope of MnFeNiCuZn–noMg-600 °C suggests that it is comparable to those of other existing highly efficient catalysts. The ECSA values are presented in Figure 3c and are listed in Table 2 for the 600 °C series. The ECSA plays a pivotal role in the field of electrocatalysis, particularly in reactions like the OER which is of paramount importance for various energy conversion and storage technologies, including water electrolysis.<sup>65,66</sup> The ECSA values range between 12.2 and 36.8 cm<sup>2</sup> for the 600 °C sample series, representing moderate values compared, for example, to the reported 65 cm<sup>2</sup> of N–NiCo<sub>2</sub>O<sub>4</sub>@C@NF.<sup>49</sup> The favorable electrocatalytic properties of the series despite their modest ECSAs suggest that these compositionally complex samples may have high intrinsic performance relative to previously reported cobaltite-based bifunctional catalysts. Among the multimetal oxide series studied here, it is notable that the MnFeNiCuZn–noMg-600 °C stands out with the highest ECSA value in the context of the OER, indicative of a significantly larger active surface area available for electrochemical reactions. This implies the presence of a higher density of catalytic sites, rendering the material exceptionally efficient in facilitating the OER process.<sup>67</sup> The composition of MnFeNiCuZn–noMg likely provides a synergistic combination of metal oxides that create a unique surface structure and electronic environment, leading to the observed higher ECSA value. The  $C_{\text{DL}}$  values of the different catalyst compositions

**Table 2. OER [Overpotential  $\eta$ , Tafel Slope, ECSA, Substrate, and Drop-Cast Mass (Mass Loading)] and ORR [Onset Potential  $E_0$ , Number of Electrons  $n$ , %  $H_2O_2$ , Substrate, and Drop-Cast Mass (Mass Loading)] Catalytic Activities of the Electrocatalysts Involved in This Work Compared to the Values from Selected Benchmark Catalysts<sup>a</sup>**

sample	OER $\eta$ (mV) @ 10 (mA cm <sup>-2</sup> )	OER Tafel (mV dec <sup>-1</sup> )	OER ECSA (cm <sup>2</sup> )	OER substrate	OER mass loading (mg cm <sup>-2</sup> )	ORR $E_0$ (V)	ORR $n$ @ 0.3 V	ORR % $H_2O_2$ @ 0.3 V	ORR substrate	ORR mass loading (mg cm <sup>-2</sup> )
Al–Ni–Co–Ru–Mo–Cr–Fe–Ti <sup>22</sup>	240	51.3		GC	0.0283 <sup>b</sup>	0.97			GC	0.0283 <sup>b</sup>
N–NiCo <sub>2</sub> O <sub>4</sub> @C@NF <sup>49</sup>	242	86	65	NF	28	0.90	3.8	6.7	GC	0.2551
AlNiCoFeCrMoV/Co–N–C <sup>26</sup>	257			GC		0.92			GC	
MnFeNiCuZn–noMg <sup>This work</sup>	260	68	36.8	CC	4.5	0.91	3.96	4.8	GC	1.3
MgMnFeNiCu–noZn <sup>This work</sup>	264	72	33.4	CC	4.5	0.84	3.21	8.2	GC	1.3
MgMnNiCuZn–noFe <sup>This work</sup>	268	84	29.1	CC	4.5	0.88	3.85	6.4	GC	1.3
Ni <sub>1.5</sub> Co <sub>1.5</sub> O <sub>4</sub> <sup>19</sup>	275	54		CC	1.5	0.92			GC	0.15
MgFeNiCuZn–noMn <sup>This work</sup>	288	96	23.78	CC	4.5	0.79	3.10	8.6	GC	1.3
MgMnFeCuZn–noNi <sup>This work</sup>	306	112	17.2	CC	4.5	0.88	3.90	5.1	GC	1.3
MgMnFeNiZn–noCu <sup>This work</sup>	310	132	12.2	CC	4.5	0.87	3.34	7.4	GC	1.3
Fe <sub>0.1</sub> Ni <sub>0.9</sub> Co <sub>2</sub> O <sub>4</sub> <sup>24</sup>	380			GC	0.2	0.85			GC	0.2

<sup>a</sup>The substrates are coded: carbon cloth (“CC”), nickel foam (“NF”), and glassy carbon (“GC”). <sup>b</sup>The mass loading is reported for Ru metal only for this sample.

were also compared (as shown in Table S2), which shows a similar trend as the ECSA. Another crucial parameter to consider is the RF, which characterizes the surface roughness of the catalyst composite and can have an impact on the observed catalytic characteristics. An increase in the ECSA leads to a higher surface RF, serving as an additional determinant affecting catalytic activity. This is typically beneficial because a rough catalytic surface exposes more catalytic sites to the electrolyte. The RF value determined for the MnFeNiCuZn–noMg-600 °C electrode (130.03) surpasses that of other synthesized compositions, aligning with the enhanced OER catalytic activity observed in the MnFeNiCuZn–noMg-600 °C sample. The substrate and drop-cast mass (mass loading) for OER and ORR studies are summarized in Table 2 as well. These choices were made to optimize the electrochemical conditions for each reaction, ensuring a reliable and controlled experimental setup.

The polarization curves for the ORR recorded at the rotation rate of 1600 rpm are shown in Figure 3d. Additional polarization curves at 400, 800, 1200, and 2000 rpm can be found in Figure S2. Among the various multimetal oxide catalysts studied, the MnFeNiCuZn–noMg-600 °C electrode emerged as the standout performer. Its diffusion current densities were found to be remarkably high, akin to those achieved with the industry-standard 20% Pt/C catalyst.<sup>66</sup> Notably, the onset potentials observed for MnFeNiCuZn–noMg-600 °C were 0.91 V vs RHE, indicating its excellent catalytic activity for the ORR. Moreover, this electrode exhibited a diffusion-limiting current density of 2.94 mA cm<sup>-2</sup>, surpassing the performance of all other electrocatalysts investigated in this study. The various diffusion-limiting currents observed in different catalysts can be attributed to their unique electronic structures and corresponding redox properties. Catalysts with higher intrinsic activity often display more prominent limiting diffusion currents. Additionally, the chemical composition of a catalyst, especially when alloyed with other elements, significantly influences the diffusion current density during the ORR. Variations in crystallographic facets, defects, or the presence of specific active sites can lead to differences in ORR kinetics, thereby influencing the limiting diffusion current.

The electron transfer and hydrogen peroxide yields (%  $H_2O_2$ ) of the ORR were also investigated (results for sample MnFeNiCuZn–noMg-600 °C are shown in Figure S3). The %  $H_2O_2$  generated is lower than 6% over a potential range of 0.2 to 0.8 V vs RHE (it is 4.8% at 0.3 V). This is lower than that reported for the highly performing N–NiCo<sub>2</sub>O<sub>4</sub>@C@NF,<sup>49</sup> which remains lower than 8% over the potential range of 0.2 to 0.7 V vs RHE (and is 6.7% at 0.3 V). Furthermore, the number of electrons transferred at 0.3 V vs RHE ranged between 3.1 to 3.96 for the 600 °C series electrocatalysts in this work, suggesting a predominant four-electron pathway for the ORR. The parallel trends observed in the fitted lines in the Koutecky–Levich plots (K–L, as shown in Figure S4) imply that the ORR follows similar electron-transfer pathways at various potentials. This suggests that the underlying mechanisms governing the ORR remain consistent across different conditions and potentials. Extracted values for the OER overpotential, Tafel slope, and ECSA, as well as the ORR onset potential, number of electrons transferred ( $n$ ), and %  $H_2O_2$  production at 0.3 V vs RHE, are summarized in Table 2 for the 600 °C sample series and selected benchmark electrocatalysts, arranged in increasing order of the OER overpotential.

In essence, MnFeNiCuZn–noMg-600 °C has demonstrated exceptional potential as a high-performance bifunctional catalyst, particularly in the context of the ORR and the OER under alkaline conditions. Its impressive electrocatalytic properties, characterized by high current densities and favorable onset potentials, make it a promising candidate for integrated electrolyzer and fuel cell systems.

#### Stability of MnFeNiCuZn–noMg-600 °C

The long-term stability of electrocatalysis processes in alkaline medium for Co-based spinel catalysts will be important for determining their overall suitability for applications.<sup>9</sup> The long-term stability of MnFeNiCuZn–noMg-600 °C, the best-performing bifunctional OER and ORR catalyst in our series, was assessed using chronoamperometry where a three-electrode setup was employed with a catalyst-coated carbon cloth as the working electrode, graphite rod as the counter electrode, and Ag/AgCl as the reference electrode, where a constant potential was applied and the resulting current density was measured over time (the results of the 22 h test are shown in Figure 4a). The increase in current density observed with

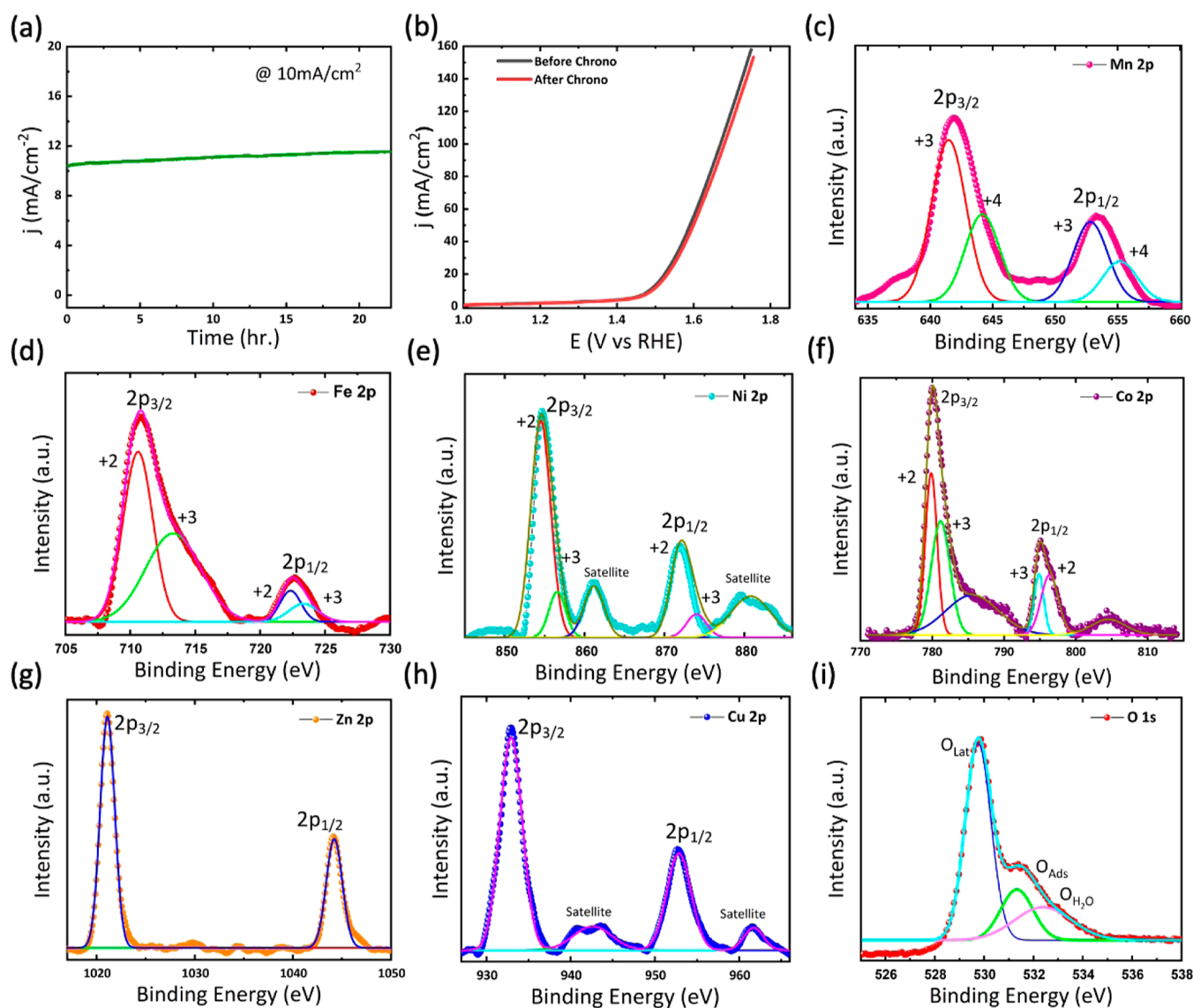


**Figure 4.** (a) Chronoamperometry plot of the catalyst MnFeNiCuZn–noMg–600 °C, as shown to maintain the current density 10 mA cm<sup>-2</sup> over 22 h for the OER. (b) LSV polarization curves of sample MnFeNiCuZn–noMg–600 °C before and after chronoamperometry. The before OER XPS spectra of (c) Mn 2p, (d) Fe 2p, (e) Ni 2p, (f) Co 2p, (g) Zn 2p, (h) Cu 2p, and (i) O 1s are for the MnFeNiCuZn–noMg–600 °C electrode. The comparison of XPS spectra before and after the OER can be found in Figure S5.

time in the chronoamperometry plot can be attributed to surface reconstruction effects. For instance, an evolving surface morphology may expose new catalytic sites or enhance the ECSA. This, in turn, facilitates more efficient OER kinetics and contributes to the observed rise in the current density over time. The electrode exhibited excellent stability with no degradation of current density. Furthermore, Figure 4b illustrates the lack of change in the LSV curves of the OER before and after the 22 h chronoamperometry test, indicating promising stability of MnFeNiCuZn–noMg–600 °C in alkaline media.

Additionally, XPS measurements were conducted on MnFeNiCuZn–noMg–600 °C before and after the OER to analyze changes in surface element configurations and electronic states. The XPS data collected before OER are presented in Figure 4c–i for elements Mn, Fe, Ni, Co, Zn, Cu, and O, respectively. The peaks in the XPS spectra can be attributed to (c) Mn 2p<sub>3/2</sub> and Mn 2p<sub>1/2</sub>, (d) Fe 2p<sub>3/2</sub> and Fe 2p<sub>1/2</sub>, (e) Ni 2p<sub>3/2</sub> and Ni 2p<sub>1/2</sub>, (f) Co 2p<sub>3/2</sub> and Co 2p<sub>1/2</sub>, (g)

Zn 2p<sub>3/2</sub> and Zn 2p<sub>1/2</sub>, (h) Cu 2p<sub>3/2</sub> and Cu 2p<sub>1/2</sub>, and (i) O 1s. In Figure 4c, the high-resolution XPS spectra of the Mn 2p peak are depicted. The Mn 2p peak exhibits a doublet, attributed to spin–orbit splitting, with two distinct states, 3/2 and 1/2. These states display varying binding energies at 641.8 and 653.2 eV. In the Fe 2p spectrum (as depicted in Figure 4d), the peaks observed at 710.2 and 723.9 eV are indicative of bivalent iron (Fe<sup>2+</sup>), while the peaks at 712.8 and 724.1 eV are assigned to trivalent iron (Fe<sup>3+</sup>). The Ni 2p XPS spectrum shown in Figure 4e reveals key information about the chemical and oxidation states of Ni within the material. The specific binding energies of the Ni 2p<sub>3/2</sub> and Ni 2p<sub>1/2</sub> core level peaks were identified at 854.2 and 871.7 eV, respectively. The Ni 2p<sub>3/2</sub> and Ni 2p<sub>1/2</sub> peaks represent transitions of electrons from the 2p energy level to the 3/2 and 1/2 spin–orbit states, providing insights into the electronic configuration of Ni in the sample. Notably, accompanying these main peaks were satellite peaks observed at 861.4 and 880.1 eV, associated with the Ni 2p<sub>3/2</sub> and Ni 2p<sub>1/2</sub> core levels, respectively. The presence of

satellite peaks is significant because it suggests that the material comprises additional electronic transitions and interactions. The detection of satellite peaks at 861.4 and 880.1 eV in this context shows that Ni is involved in a +2 oxidation state within the main lattice. In Figure 4f, the XPS spectrum analysis has revealed that the primary metal peaks in the Co  $2p_{3/2}$  and Co  $2p_{1/2}$  regions exhibit binding energies at 780.2 and 796.1 eV, respectively. Additionally, within both the Co  $2p_{3/2}$  and Co  $2p_{1/2}$  regions, there are satellite peaks observed on the side with higher binding energy relative to the main peak of each region. This observation supports the confirmation that the oxidation state of Co is predominantly +2. The higher binding energy of the satellite peaks relative to the main peaks within the Co  $2p$  regions aligns with the characteristics expected for Co in the +2 state.<sup>68</sup> These two satellite peaks also indicate the presence of additional electronic states associated with cobalt atoms. The satellite peak can arise from charge redistribution or electronic transitions within the cobalt atoms. Charge redistribution implies a rearrangement of electrons within the cobalt atoms, potentially influenced by factors such as the local environment, the presence of neighboring atoms, or specific surface conditions. This redistribution of charge can lead to the creation of additional electronic states, contributing to the appearance of a satellite peak. In Figure 4g, the XPS spectrum for Zn  $2p$  illustrates the binding energies of Zn  $2p_{3/2}$  at approximately 1021.6 eV and Zn  $2p_{1/2}$  centered around 1044.1 eV. It indicates a single +2 valence. XPS spectra collected after the OER are shown in Figure S5. There are no significant shifts observed in the binding energies of the Mn, Fe, Ni, Co, and Zn elements after OER activity. Negligible binding energy shifts observed for most of the sample metal ions indicate a maintenance of stable oxidation states during the OER without undergoing substantial chemical transformations or degradation. It should be noted that in OER electrocatalysis, it is expected that oxyhydroxide species will form at the local catalytic site through the catalyst activation step. The lack of observable shifts however indicates that there is no bulk conversion to oxyhydroxide species or significant alterations in the chemical states of these elements during extended OER activity. Elements like Mn, Fe, Ni, Co, and Zn may exhibit different inherent redox potentials, making them less susceptible to changes in oxidation states during electrochemical processes. There are two marked changes in the XPS spectra before and after the OER (beyond differences in intensities, attributed to the measurements being completed in different areas of the sample): (1) In Figure 4h, the core-level and shakeup satellite lines of Cu  $2p$  are presented. The Cu  $2p_{3/2}$  and  $2p_{1/2}$  core levels are situated at approximately 933.2 and 952.9 eV, respectively. However, in the XPS spectra after the OER, Figure S5f, Cu<sup>1+</sup> peaks appear around 932.1 eV after the OER in addition to the Cu<sup>2+</sup> peaks initially present (as shown in Figure S5f). More careful XPS analysis has revealed that Cu is present in +1 and +2 oxidation states even in the sample before OER measurement. Hence, the presence of Cu<sup>1+</sup> in the sample is primarily due to mixed oxidation state in the pristine sample and does not change significantly after the OER. Furthermore, to substantiate the dominance of Cu<sup>2+</sup> oxidation, our analysis considered the presence of a satellite peak around 943.2 eV. The identification of this satellite peak is particularly significant as it serves as a spectral indicator affirming the prevalence of Cu<sup>2+</sup> oxidation states.<sup>69,70</sup> (2) The O  $1s$  peak at 529 eV in Figure 4i indicates the presence of O<sup>2-</sup> within a metal oxide lattice (O<sub>Lat</sub>), while the peak at 531 eV

suggests the presence of adsorbed oxygen-containing species (O<sub>Ads</sub>). This peak's intensity is commonly utilized to measure the concentration of oxygen vacancies within the surface oxide lattice. The small peak observed at 533 eV is associated with water adsorption (O<sub>H<sub>2</sub>O</sub>).<sup>71</sup> This latter peak disappears after the OER activity, indicating a loss of adsorbed water. The lack of changes in the case of Mn, Fe, Ni, Co, and Zn indicates a stable surface chemistry of this catalyst. The CCO catalyst may possess a robust surface structure that preserves the oxidation states of the constituent elements, even in the presence of highly oxidative OER conditions. This stability could arise from the synergistic interactions among the different metal species, forming a protective layer that prevents excessive oxidation or reduction.

### Tunability through Cation Selection and Postannealing

With the implementation of the straightforward LTST synthesis method, substantial potential exists for enhancing the catalytic properties of bifunctional OER and ORR AC<sub>2</sub>O<sub>4</sub> electrocatalysts through cation selection and reaction parameter optimization. Trends in crystallinity, phase purity, and morphology are shown for various sample thermal treatments for the MnFeNiCuZn–noMg composition in Figure 2. Panel (b) displays the XRD patterns of the series, including the 400, 600, 800, and 1000 °C samples. Rietveld refinements were completed to identify phases present, crystallite size (CS) and cation site inversion parameter ( $\gamma$ ). In the case of the MnFeNiCuZn–noMg series, the 400 °C sample contains a processing product impurity CoCl<sub>2</sub>·2H<sub>2</sub>O (labeled as “h”), while the 800 °C sample contains a small amount of CuO (“c”). The 1000 °C sample exhibits CuO, rock salt (“r”), and secondary spinel (“s”) impurities. Only the 600 °C sample is composed purely of a single spinel phase. A summary of the phase purity results achieved for all samples is given in Table 1.

SEM results for the MnFeNiCuZn–noMg composition series are displayed in Figure 2c. The 400 °C sample exhibits a wide particle size distribution (with both large octahedral shaped particles and smaller spheroidal agglomerates). EDS analysis presented in Figure S6 reveals that the sample exhibits homogeneous distributions of all analyzed elements at the resolution probed. Higher post-treatment temperatures (600 and 800 °C) lead to larger particle sizes and a more homogeneous particle size distribution, consistent with the results from Rietveld refinements.<sup>62</sup> The 1000 °C treated sample displays particle sizes in the micrometer-scale (bulk) range. High-resolution SEM was conducted on the heat treatment series of two other compositions: MgMnFeCuZn–noNi and MgFeNiCuZn–noMn, as illustrated in Figure S7. Similar observations are made regarding the morphology and particle size distribution trends. Overall, these findings provide valuable insights into the modification of the sample purity and morphology achieved through different post-treatment temperatures.

As previously mentioned (also shown in Figure S1a), the MnFeNiCuZn–noMg-400 °C exhibits the poorest OER performance as compared to 600, 800, and 1000 °C postannealed samples. Remarkably, even though the 1000 °C series exhibits micrometer scale particle sizes, they demonstrate excellent OER performance (comparable to the 600 °C sample series). On the other hand, the 800 °C series exhibits a more uniform particle size distribution but falls short of the performance observed in the 1000 °C series. These trends suggest that particle size is not the predominant factor in

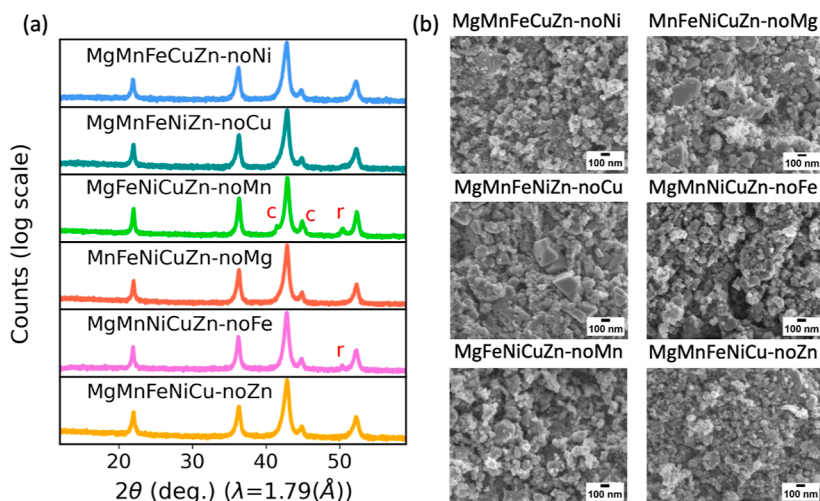


**Figure 5.** XRD patterns of (a) 600 °C series of MgMnFeCuZn–noNi, MgMnFeNiZn–noCu, MgFeNiCuZn–noMn, MnFeNiCuZn–noMg, MgMnNiCuZn–noFe, and MgMnFeNiCu–noZn samples. Impurities are coded: tenorite CuO (“c”) and rock salt (“r”). SEM images in (b) reveal the morphology of the samples in (a).

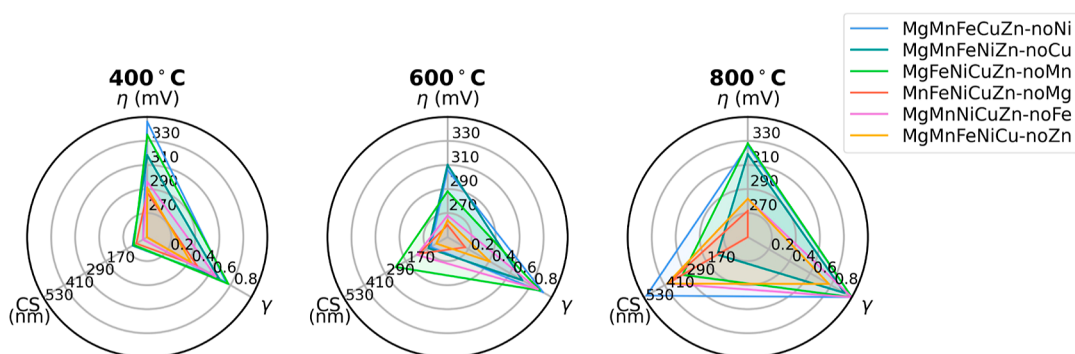


**Figure 6.** Overpotential ( $\eta$ , measured at 10 mA cm<sup>-2</sup>) of OER, CS (nm), and cation site inversion ( $\gamma$ ) for all six compositions ( $SA_{1/3}$ )Co<sub>2</sub>O<sub>4</sub>, MgMnFeCuZn–noNi (blue), MgMnFeNiZn–noCu (teal), MgFeNiCuZn–noMn (green), MnFeNiCuZn–noMg (orange), MgMnNiCuZn–noFe (pink), and MgMnFeNiCu–noZn (yellow). Left to right, correlations are depicted for the as-prepared samples (400 °C), and samples postannealed at 600 and 800 °C.

determining the OER performance and that postannealing is an effective tuning parameter for CCO nanocatalysts in this series. Further investigation is required to determine whether the higher 600 °C performance trend can be attributed to phase purity, a tuning toward cation short-range order at the atomic or nanoscale, a morphological improvement facilitated by the unique cation diffusion processes in compositionally complex systems, or some other effects.

The XRD patterns and SEM images of the 600 °C sample series are compared in Figure 5a,b, respectively. The XRD patterns reveal that MgFeNiCuZn–noMn-600 °C and MgMnNiCuZn–noFe-600 °C samples have small impurities, while the remaining four samples appear to be in a single phase state. The SEM images of all compositions reveal qualitatively similar particle size distributions and morphologies. These observations together with the noted variation in the OER and ORR performance across the compositional series suggest the varying combination of multimetal cations, referred to as “cation selection” in this study, plays an important role. Interestingly, the samples MnFeNiCuZn–noMg, MgMnNiCuZn–noFe, and MgMnFeNiCu–noZn have better bifunctional OER and ORR catalytic activity, relative to MgMnFeCuZn–noNi, MgMnFeNiZn–noCu, and MgFeNiCuZn–noMn. This suggests that Mn, Cu, and Ni play a significant

role in both the OER and ORR. This departs from the catalytic activity trends observed for the OER in the end member compositions in alkaline solution, which reflects the order: ZnCo<sub>2</sub>O<sub>4</sub> > NiCo<sub>2</sub>O<sub>4</sub> > FeCo<sub>2</sub>O<sub>4</sub> > Co<sub>3</sub>O<sub>4</sub> > MnCo<sub>2</sub>O<sub>4</sub>.<sup>72</sup> Thus, the work herein provides another example of the multimetal enhancement effects observed in compositionally complex electrocatalysts. By comparing CCOs with each distinct combination of five out of six selected cations occupying the A site (ACo<sub>2</sub>O<sub>4</sub>), the relative influence of each metal cation on the bifunctional OER and ORR performance can be efficiently screened. This approach allowed us to collect valuable performance information through a small subset of possible compositions. These findings indicate a promising pathway for designing new materials in the vast design space available for CCOs. In our future work, we will investigate the potential of improving the bifunctional OER and ORR activities of the CCO ACo<sub>2</sub>O<sub>4</sub> family by exploring various combinations of only Mn, Cu, and Ni incorporation.

Beyond cation selection, our work demonstrates that electrocatalytic properties in the CCO ACo<sub>2</sub>O<sub>4</sub> family can be influenced through processing variations in the LTST synthesis method. A series of spider plots corresponding to increasing postannealing temperature is given in Figure 6, created to

illustrate the complex correlations between the measured OER overpotential ( $\eta$ , mV), crystalline domain size determined from Rietveld analysis (CS, nm), and cation site inversion determined from Rietveld analysis ( $\gamma$ ) for the compositions studied (the analysis involved in determining the latter two parameters are described in detail in our previous work<sup>62</sup>). As the processing temperature increases from 400 to 800 °C (the series of spider plots from left to right),  $\eta$  initially decreases and then increases (this correlation is provided as a separate plot in Figure S1a). As may be expected, the average crystallinity of all samples increases with increasing annealing temperature, but they do so at varying rates. Interestingly, the cation site inversion parameter,  $\gamma$ , is also revealed to vary significantly with heat treatment. For all compositions treated at 400 °C,  $\gamma$  is near 2/3 (representing a near random spinel structure where A-site cations and Co<sup>3+</sup> are present in 1/3 and 2/3 ratios on both the tetrahedral and octahedral sites, respectively). For most compositions,  $\gamma$  approaches 1 at higher temperatures (representing an inverse spinel structure with all A-site cations occupying the octahedral site and half of the Co<sup>3+</sup> occupying the tetrahedral site) as the temperature increases. The highest performing OER catalyst, MnFeNiCuZn–noMg, is an exception: it exhibits a decrease in  $\gamma$  with higher annealing temperatures and approaches 0 at 800 °C (representing a normal spinel structure with A-site cations only occupying the tetrahedral site and Co<sup>3+</sup> only occupying the octahedral site). These correlations are shown individually in Figure S1c for further clarity. To be clear, only the simplest normal, inverse, and random site models were considered (with all the A atom occupancies constrained to be equivalent on each spinel cation site, and each cation site constrained to have a total occupancy of 1) due to the relative insensitivity of XRD to shared transition-metal site occupancies.<sup>62</sup> Nonetheless, the trends from the Rietveld refinement indicate significant changes in the cation site ordering that vary across the series. The details of the Rietveld refinement with the “continuous lattice” model for the 600 °C sample series are included in Table S3, which provides information about  $R_{\text{wp}}$ , median of the lattice parameter ( $a_m$ , Å), crystallite domain size (CS), cation site inversion parameter ( $\gamma$ ), and atomic position of oxygen ( $u$ ). The isotropic atomic displacement parameters ( $U_{\text{iso}}$ , Å<sup>2</sup>) for the tetrahedral site, octahedral site, and oxygen were fixed as 0.005, 0.005, and 0.010 Å<sup>2</sup>, respectively, for all compositions. At the same time, the surface oxidation states obtained from XPS measurements indicate a partial inverse spinel structure, creating a complex and intriguing scenario. Extended X-ray absorption fine structure, X-ray absorption near edge structure, nuclear magnetic resonance, Mössbauer spectroscopy, neutron diffraction, or other complementary measurements would be necessary to study the cation site occupancy trends in fine detail. Finally, the comparison between  $\eta$  and CS, and  $\eta$  and  $\gamma$  for the series do not illicit clear trends (the relationships are shown individually in Figure S1b,d, respectively). Rather, it can be inferred that morphology, chemistry, and thermal history are interconnected tuning factors in the electrocatalytic performance of the CCO ACo<sub>2</sub>O<sub>4</sub> samples studied here.

Overall, the enhanced OER efficiency and effective ORR activity observed for MnFeNiCuZn–noMg-600 °C can be attributed to a synergistic interplay of several key elements. MnFeNiCuZn–noMg (along with other compositions reported in this study) benefits from a diverse array of transition-metal cations, each of which can act as a potential catalytic site

with varying degrees of electrochemical tunability. This amalgamation of metal ions creates a unique and advantageous chemical environment for catalysis, wherein each metal may contribute its own catalytic properties, as well as influence the local electron density around the neighboring cations. The specific chemical environments and the OER activities are shown to be impacted by thermal annealing, revealing an additional tuning parameter in optimizing efficient CCO catalysts. Finally, the MnFeNiCuZn–noMg-600 °C catalyst possesses a substantial ECSA. A larger electrochemical surface area equates to more active sites available for electrocatalysis, leading to higher current density. Hence, the outstanding OER activity of MnFeNiCuZn–noMg-600 °C is most likely the outcome of a harmonious interplay between its diverse composition, expansive surface area, unique (amalgamated) electronic structure, and the electrochemical tunability of the catalytic site. This intricate combination renders this catalyst exceptionally effective for the OER and indicates a promising direction for simultaneously improving ORR.

## CONCLUSIONS

Nano CCO ( $5A_{1/5}$ )Co<sub>2</sub>O<sub>4</sub> phases made by the LTST method show great promise as tunable bifunctional electrocatalysts for water splitting technologies. The sample MnFeNiCuZn–noMg-600 °C shows an exceptional overpotential for the OER at 260 mV at 10 mA cm<sup>-2</sup> and excellent onset potential, 0.91 V, for the ORR. It was demonstrated that thermal heat treatment of nanostructured phases can be used to drive cation diffusion and “tune” the structures toward high activity. The results presented suggest that further tuning of morphology, cation short-range ordering/nanostructuring, and composition will lead to further enhancement in this family of cobaltites. Furthermore, based on the compositional screening herein, it is anticipated that exchanging noncatalytically active cations such as Mg for larger proportions of catalytically active cations, such as Mn, Cu and Ni, will result in further performance enhancements. Overall, this work displays the great potential of LTST to produce nano CCOs for bifunctional catalytic design. The reaction route provides a straightforward way to screen potential CCO compositions for catalytic activity, explore the potential synergistic effects of incorporating many metal cations, and understand the impact of thermal annealing and associated cation short-range order. These directions will be explored in future work.

## ASSOCIATED CONTENT

### Supporting Information

The Supporting Information is available free of charge at <https://pubs.acs.org/doi/10.1021/acsmaterialsau.3c00088>.

Excellent bifunctional oxygen evolution and reduction electrocatalysts ( $5A_{1/5}$ )Co<sub>2</sub>O<sub>4</sub> and their tunability: comparisons between overpotential (mV) at 10 mA cm<sup>-2</sup> for the OER and heat treatment temperatures, crystalline domain size (nm), and cation site inversion ( $\gamma$ ), as well as a comparison between  $\gamma$  and heat treatment temperature; LSV of ORR at different rotating speeds; H<sub>2</sub>O<sub>2</sub> yields and electron-transfer numbers for the ORR of MnFeNiCuZn–noMg-600 °C; K–L plots at different electrode potentials for MnFeNiCuZn–noMg-600 °C; before and after OER XPS spectra comparison; SEM/EDS maps of sample MnFeNiCuZn–noMg-400 °C; SEM images of MgMnFeCuZn–noNi and MgFe-

NiCuZn–noMn processed with different heat treatment temperatures; information of substrate and drop-cast mass (mass loading) of OER and ORR catalytic measurements;  $C_{DL}$  comparison for the 600 °C sample series; and details of Rietveld refinement of the 600 °C sample series (PDF)

## AUTHOR INFORMATION

### Corresponding Author

**Katharine Page** – Department of Materials Science and Engineering, Institute for Advanced Materials and Manufacturing, University of Tennessee, Knoxville, Tennessee 37996, United States; Neutron Scattering Division, Oak Ridge National Laboratory, Oak Ridge, Tennessee 37831, United States; [orcid.org/0000-0002-9071-3383](https://orcid.org/0000-0002-9071-3383); Email: [kpage10@utk.edu](mailto:kpage10@utk.edu)

### Authors

**Xin Wang** – Department of Materials Science and Engineering, Institute for Advanced Materials and Manufacturing, University of Tennessee, Knoxville, Tennessee 37996, United States; [orcid.org/0000-0001-6769-2185](https://orcid.org/0000-0001-6769-2185)

**Harish Singh** – Department of Chemistry, Missouri University of Science and Technology, Rolla, Missouri 65409, United States

**Manashi Nath** – Department of Chemistry, Missouri University of Science and Technology, Rolla, Missouri 65409, United States; [orcid.org/0000-0002-5058-5313](https://orcid.org/0000-0002-5058-5313)

**Kurt Lagemann** – Department of Chemistry, Missouri University of Science and Technology, Rolla, Missouri 65409, United States

Complete contact information is available at: <https://pubs.acs.org/10.1021/acsmaterialsau.3c00088>

### Notes

The authors declare no competing financial interest.

## ACKNOWLEDGMENTS

K.P. gratefully acknowledges financial support from NSF-DMR-2145174. Material synthesis efforts by Xin Wang were supported in part by UT-ORII Seed Funding. M.N. also acknowledges support from NSF-CAS-2155175. XRD data, SEM images, and EDS maps were collected at Diffraction and Microscopy Core Facilities at the Institute for Advanced Materials and Manufacturing (IAMM) at the University of Tennessee, Knoxville. The authors gratefully acknowledge Dr. Michael Koehler for his assistance with XRD measurements reported in this work.

## REFERENCES

- (1) Zhang, B.; Zhang, S.-X.; Yao, R.; Wu, Y.-H.; Qiu, J.-S. Progress and prospects of hydrogen production: Opportunities and challenges. *J. Electron. Sci. Technol.* **2021**, *19*, 100080.
- (2) Dresp, S.; Strasser, P. *Metal Oxide-Based Nanostructured Electrocatalysts for Fuel Cells, Electrolyzers, and Metal-Air Batteries*; Elsevier, 2021; pp 83–103.
- (3) Maiyalagan, T.; Jarvis, K. A.; Therese, S.; Ferreira, P. J.; Manthiram, A. Spinel-type lithium cobalt oxide as a bifunctional electrocatalyst for the oxygen evolution and oxygen reduction reactions. *Nat. Commun.* **2014**, *5*, 3949–3958.
- (4) Wang, Y.; Zheng, X.; Wang, D. Design concept for electrocatalysts. *Nano Res.* **2022**, *15*, 1730–1752.

- (5) Zheng, X.; Yang, J.; Xu, Z.; Wang, Q.; Wu, J.; Zhang, E.; Dou, S.; Sun, W.; Wang, D.; Li, Y. Ru–Co pair sites catalyst boosts the energetics for the oxygen evolution reaction. *Angew. Chem., Int. Ed.* **2022**, *134*, No. e202205946.

- (6) Huang, Z.-F.; Wang, J.; Peng, Y.; Jung, C.-Y.; Fisher, A.; Wang, X. Design of efficient bifunctional oxygen reduction/evolution electrocatalyst: recent advances and perspectives. *Adv. Energy Mater.* **2017**, *7*, 1700544.

- (7) Li, A.; Kong, S.; Guo, C.; Ooka, H.; Adachi, K.; Hashizume, D.; Jiang, Q.; Han, H.; Xiao, J.; Nakamura, R. Enhancing the stability of cobalt spinel oxide towards sustainable oxygen evolution in acid. *Nat. Catal.* **2022**, *5*, 109–118.

- (8) Zhao, Q.; Yan, Z.; Chen, C.; Chen, J. Spinel: controlled preparation, oxygen reduction/evolution reaction application, and beyond. *Chem. Rev.* **2017**, *117*, 10121–10211.

- (9) Li, S.; Hao, X.; Abudula, A.; Guan, G. Nanostructured Co-based bifunctional electrocatalysts for energy conversion and storage: current status and perspectives. *J. Mater. Chem. A* **2019**, *7*, 18674–18707.

- (10) Ma, S.; Sun, L.; Cong, L.; Gao, X.; Yao, C.; Guo, X.; Tai, L.; Mei, P.; Zeng, Y.; Xie, H.; et al. Multiporous MnCo<sub>2</sub>O<sub>4</sub> microspheres as an efficient bifunctional catalyst for nonaqueous Li–O<sub>2</sub> batteries. *J. Phys. Chem. C* **2013**, *117*, 25890–25897.

- (11) Lee, D. U.; Kim, B. J.; Chen, Z. One-pot synthesis of a mesoporous NiCo<sub>2</sub>O<sub>4</sub> nanoplatelet and graphene hybrid and its oxygen reduction and evolution activities as an efficient bi-functional electrocatalyst. *J. Mater. Chem. A* **2013**, *1*, 4754–4762.

- (12) Jin, C.; Lu, F.; Cao, X.; Yang, Z.; Yang, R. Facile synthesis and excellent electrochemical properties of NiCo<sub>2</sub>O<sub>4</sub> spinel nanowire arrays as a bifunctional catalyst for the oxygen reduction and evolution reaction. *J. Mater. Chem. A* **2013**, *1*, 12170–12177.

- (13) Cao, X.; Jin, C.; Lu, F.; Yang, Z.; Shen, M.; Yang, R. Electrochemical properties of MnCo<sub>2</sub>O<sub>4</sub> spinel bifunctional catalyst for oxygen reduction and evolution reaction. *J. Electrochem. Soc.* **2014**, *161*, H296–H300.

- (14) Serov, A.; Andersen, N. I.; Roy, A. J.; Matanovic, I.; Artyushkova, K.; Atanassov, P. CuCo<sub>2</sub>O<sub>4</sub> ORR/OER bi-functional catalyst: influence of synthetic approach on performance. *J. Electrochem. Soc.* **2015**, *162*, F449–F454.

- (15) Menezes, P. W.; Indra, A.; Sahraie, N. R.; Bergmann, A.; Strasser, P.; Driess, M. Cobalt–manganese-based spinels as multi-functional materials that unify catalytic water oxidation and oxygen reduction reactions. *ChemSusChem* **2015**, *8*, 164–171.

- (16) Devaguptapu, S. V.; Hwang, S.; Karakalos, S.; Zhao, S.; Gupta, S.; Su, D.; Xu, H.; Wu, G. Morphology control of carbon-free spinel NiCo<sub>2</sub>O<sub>4</sub> catalysts for enhanced bifunctional oxygen reduction and evolution in alkaline media. *ACS Appl. Mater. Interfaces* **2017**, *9*, 44567–44578.

- (17) Wang, W.; Kuai, L.; Cao, W.; Huttula, M.; Ollikkala, S.; Ahopelto, T.; Honkanen, A.-P.; Huotari, S.; Yu, M.; Geng, B. Mass-Production of Mesoporous MnCo<sub>2</sub>O<sub>4</sub> Spinel with Manganese (IV)- and Cobalt (II)-Rich Surfaces for Superior Bifunctional Oxygen Electrocatalysis. *Angew. Chem.* **2017**, *129*, 15173–15177.

- (18) Béjar, J.; Álvarez-Contreras, L.; Ledesma-García, J.; Arjona, N.; Arriaga, L. Electrochemical evaluation of Co<sub>3</sub>O<sub>4</sub> and NiCo<sub>2</sub>O<sub>4</sub> rosettes-like hierarchical spinel as bifunctional materials for oxygen evolution (OER) and reduction (ORR) reactions in alkaline media. *J. Electroanal. Chem.* **2019**, *847*, 113190.

- (19) Zhao, J.; He, Y.; Wang, J.; Zhang, J.; Qiu, L.; Chen, Y.; Zhong, C.; Han, X.; Deng, Y.; Hu, W. Regulating metal active sites of atomically-thin nickel-doped spinel cobalt oxide toward enhanced oxygen electrocatalysis. *Chem. Eng. J.* **2022**, *435*, 134261.

- (20) Liu, W.; Bao, J.; Xu, L.; Guan, M.; Wang, Z.; Qiu, J.; Huang, Y.; Xia, J.; Lei, Y.; Li, H. NiCo<sub>2</sub>O<sub>4</sub> ultrathin nanosheets with oxygen vacancies as bifunctional electrocatalysts for Zn-air battery. *Appl. Surf. Sci.* **2019**, *478*, 552–559.

- (21) Deelod, W.; Priamushko, T.; Čížek, J.; Suramitr, S.; Kleitz, F. Defect-engineered hydroxylated mesoporous spinel oxides as bifunc-

tional electrocatalysts for oxygen reduction and evolution reactions. *ACS Appl. Mater. Interfaces* **2022**, *14*, 23307–23321.

(22) Jin, Z.; Lyu, J.; Hu, K.; Chen, Z.; Xie, G.; Liu, X.; Lin, X.; Qiu, H.-J. Eight-component nanoporous high-entropy oxides with low Ru contents as high-performance bifunctional catalysts in Zn-air batteries. *Small* **2022**, *18*, 2107207.

(23) Chen, X.; Han, F.; Chen, X.; Zhang, C.; Gou, W. Cerium-Doped  $\text{CoMn}_2\text{O}_4$  Spinel as Highly Efficient Bifunctional Electro-catalysts for ORR/OER Reactions. *Catalysts* **2022**, *12*, 1122.

(24) Lu, Y.-T.; Chien, Y.-J.; Liu, C.-F.; You, T.-H.; Hu, C.-C. Active site-engineered bifunctional electrocatalysts of ternary spinel oxides,  $\text{M}_{0.1}\text{Ni}_{0.9}\text{Co}_2\text{O}_4$  (M: Mn, Fe, Cu, Zn) for the air electrode of rechargeable zinc-air batteries. *J. Mater. Chem. A* **2017**, *5*, 21016–21026.

(25) Song, W.; Ren, Z.; Chen, S.-Y.; Meng, Y.; Biswas, S.; Nandi, P.; Elsen, H. A.; Gao, P.-X.; Suib, S. L. Ni-and Mn-promoted mesoporous  $\text{Co}_3\text{O}_4$ : a stable bifunctional catalyst with surface-structure-dependent activity for oxygen reduction reaction and oxygen evolution reaction. *ACS Appl. Mater. Interfaces* **2016**, *8*, 20802–20813.

(26) Yu, T.; Xu, H.; Jin, Z.; Zhang, Y.; Qiu, H.-J. Noble metal-free high-entropy oxide/Co-NC bifunctional electrocatalyst enables highly reversible and durable Zn-air batteries. *Appl. Surf. Sci.* **2023**, *610*, 155624.

(27) Wang, Z.; Huang, J.; Wang, L.; Liu, Y.; Liu, W.; Zhao, S.; Liu, Z.-Q. Cation-tuning induced d-band center modulation on Co-based spinel oxide for oxygen reduction/evolution reaction. *Angew. Chem., Int. Ed.* **2022**, *61*, No. e202114696.

(28) Zhang, Z.; Li, J.; Qian, J.; Li, Z.; Jia, L.; Gao, D.; Xue, D. Significant Change of Metal Cations in Geometric Sites by Magnetic-Field Annealing  $\text{FeCo}_2\text{O}_4$  for Enhanced Oxygen Catalytic Activity. *Small* **2022**, *18*, 2104248.

(29) Liang, Y.; Li, Y.; Wang, H.; Zhou, J.; Wang, J.; Regier, T.; Dai, H.  $\text{Co}_3\text{O}_4$  nanocrystals on graphene as a synergistic catalyst for oxygen reduction reaction. *Nat. Mater.* **2011**, *10*, 780–786.

(30) Liu, Y.; Higgins, D. C.; Wu, J.; Fowler, M.; Chen, Z. Cubic spinel cobalt oxide/multi-walled carbon nanotube composites as an efficient bifunctional electrocatalyst for oxygen reaction. *Electrochem. Commun.* **2013**, *34*, 125–129.

(31) Zhang, C.; Antonietti, M.; Feller, T.-P. Blood ties:  $\text{Co}_3\text{O}_4$  decorated blood derived carbon as a superior bifunctional electrocatalyst. *Adv. Funct. Mater.* **2014**, *24*, 7655–7665.

(32) Zhao, A.; Masa, J.; Xia, W.; Maljusch, A.; Willinger, M.-G.; Clavel, G.; Xie, K.; Schlogl, R.; Schuhmann, W.; Muhler, M. Spinel Mn–Co oxide in N-doped carbon nanotubes as a bifunctional electrocatalyst synthesized by oxidative cutting. *J. Am. Chem. Soc.* **2014**, *136*, 7551–7554.

(33) Xu, C.; Lu, M.; Zhan, Y.; Lee, J. Y. A bifunctional oxygen electrocatalyst from monodisperse  $\text{MnCo}_2\text{O}_4$  nanoparticles on nitrogen enriched carbon nanofibers. *RSC Adv.* **2014**, *4*, 25089–25092.

(34) Ge, X.; Liu, Y.; Goh, F. W. T.; Hor, T. S. A.; Zong, Y.; Xiao, P.; Zhang, Z.; Lim, S. H.; Li, B.; Wang, X.; et al. Dual-phase spinel  $\text{MnCo}_2\text{O}_4$  and spinel  $\text{MnCo}_2\text{O}_4$ /nanocarbon hybrids for electrocatalytic oxygen reduction and evolution. *ACS Appl. Mater. Interfaces* **2014**, *6*, 12684–12691.

(35) An, T.; Ge, X.; Hor, T. S. A.; Goh, F. W. T.; Geng, D.; Du, G.; Zhan, Y.; Liu, Z.; Zong, Y.  $\text{Co}_3\text{O}_4$  nanoparticles grown on N-doped Vulcan carbon as a scalable bifunctional electrocatalyst for rechargeable zinc-air batteries. *RSC Adv.* **2015**, *5*, 75773–75780.

(36) Li, X.; Fang, Y.; Lin, X.; Tian, M.; An, X.; Fu, Y.; Li, R.; Jin, J.; Ma, J. MOF derived  $\text{Co}_3\text{O}_4$  nanoparticles embedded in N-doped mesoporous carbon layer/MWCNT hybrids: extraordinary bi-functional electrocatalysts for OER and ORR. *J. Mater. Chem. A* **2015**, *3*, 17392–17402.

(37) Liu, S.; Li, L.; Ahn, H. S.; Manthiram, A. Delineating the roles of  $\text{Co}_3\text{O}_4$  and N-doped carbon nanoweb (CNW) in bifunctional  $\text{Co}_3\text{O}_4$ /CNW catalysts for oxygen reduction and oxygen evolution reactions. *J. Mater. Chem. A* **2015**, *3*, 11615–11623.

(38) Yan, W.; Yang, Z.; Bian, W.; Yang, R.  $\text{FeCo}_2\text{O}_4$ /hollow graphene spheres hybrid with enhanced electrocatalytic activities for oxygen reduction and oxygen evolution reaction. *Carbon* **2015**, *92*, 74–83.

(39) Cao, X.; Yan, W.; Jin, C.; Tian, J.; Ke, K.; Yang, R. Surface modification of  $\text{MnCo}_2\text{O}_4$  with conducting polypyrrole as a highly active bifunctional electrocatalyst for oxygen reduction and oxygen evolution reaction. *Electrochim. Acta* **2015**, *180*, 788–794.

(40) Aijaz, A.; Masa, J.; Rösler, C.; Xia, W.; Weide, P.; Botz, A. J.; Fischer, R. A.; Schuhmann, W.; Muhler, M.  $\text{Co}@ \text{Co}_3\text{O}_4$  encapsulated in carbon nanotube-grafted nitrogen-doped carbon polyhedra as an advanced bifunctional oxygen electrode. *Angew. Chem., Int. Ed.* **2016**, *55*, 4087–4091.

(41) Xu, N.; Liu, Y.; Zhang, X.; Li, X.; Li, A.; Qiao, J.; Zhang, J. Self-assembly formation of Bi-functional  $\text{Co}_3\text{O}_4$ /MnO<sub>2</sub>-CNTs hybrid catalysts for achieving both high energy/power density and cyclic ability of rechargeable zinc-air battery. *Sci. Rep.* **2016**, *6*, 33590–33610.

(42) Dou, S.; Li, X.; Tao, L.; Huo, J.; Wang, S. Cobalt nanoparticle-embedded carbon nanotube/porous carbon hybrid derived from MOF-encapsulated  $\text{Co}_3\text{O}_4$  for oxygen electrocatalysis. *Chem. Commun.* **2016**, *52*, 9727–9730.

(43) Li, G.; Wang, X.; Fu, J.; Li, J.; Park, M. G.; Zhang, Y.; Lui, G.; Chen, Z. Pomegranate-Inspired Design of Highly Active and Durable Bifunctional Electrocatalysts for Rechargeable Metal–Air Batteries. *Angew. Chem., Int. Ed.* **2016**, *55*, 4977–4982.

(44) He, X.; Yin, F.; Yuan, S.; Liu, N.; Huang, X. Hybrid Spinel Oxides/N-Doped Reduced Graphene Oxide as Highly-Active Bifunctional Electrocatalysts for Oxygen Reduction/Evolution Reactions. *ChemElectroChem* **2016**, *3*, 1107–1115.

(45) Liu, Z.-Q.; Cheng, H.; Li, N.; Ma, T. Y.; Su, Y.-Z.  $\text{ZnCo}_2\text{O}_4$  quantum dots anchored on nitrogen-doped carbon nanotubes as reversible oxygen reduction/evolution electrocatalysts. *Adv. Mater.* **2016**, *28*, 3777–3784.

(46) Wang, J.; Wu, Z.; Han, L.; Lin, R.; Xin, H. L.; Wang, D. Hollow-Structured Carbon-Supported Nickel Cobaltite Nanoparticles as an Efficient Bifunctional Electrocatalyst for the Oxygen Reduction and Evolution Reactions. *ChemCatChem* **2016**, *8*, 736–742.

(47) Wang, X.; Li, Y.; Jin, T.; Meng, J.; Jiao, L.; Zhu, M.; Chen, J. Electrospun thin-walled  $\text{CuCo}_2\text{O}_4$ @C nanotubes as bifunctional oxygen electrocatalysts for rechargeable Zn–air batteries. *Nano Lett.* **2017**, *17*, 7989–7994.

(48) Ahmed, M. S.; Choi, B.; Kim, Y.-B. Development of highly active bifunctional electrocatalyst using  $\text{Co}_3\text{O}_4$  on carbon nanotubes for oxygen reduction and oxygen evolution. *Sci. Rep.* **2018**, *8*, 2543.

(49) Ha, Y.; Shi, L.; Yan, X.; Chen, Z.; Li, Y.; Xu, W.; Wu, R. Multifunctional electrocatalysis on a porous N-doped  $\text{NiCo}_2\text{O}_4$ @C nanonetwork. *ACS Appl. Mater. Interfaces* **2019**, *11*, 45546–45553.

(50) Chakrabarty, S.; Mukherjee, A.; Su, W.-N.; Basu, S. Improved bi-functional ORR and OER catalytic activity of reduced graphene oxide supported  $\text{ZnCo}_2\text{O}_4$  microspheres. *Int. J. Hydrogen Energy* **2019**, *44*, 1565–1578.

(51) Zhang, Y.; Chen, Z.; Tian, J.; Sun, M.; Yuan, D.; Zhang, L. Nitrogen doped  $\text{CuCo}_2\text{O}_4$  nanoparticles anchored on beaded-like carbon nanofibers as an efficient bifunctional oxygen catalyst toward zinc-air battery. *J. Colloid Interface Sci.* **2022**, *608*, 1105–1115.

(52) Wang, S.; Lu, A.; Zhong, C.-J. Hydrogen production from water electrolysis: role of catalysts. *Nano Convergence* **2021**, *8*, 4–23.

(53) Tahir, M.; Pan, L.; Idrees, F.; Zhang, X.; Wang, L.; Zou, J.-J.; Wang, Z. L. Electrocatalytic oxygen evolution reaction for energy conversion and storage: a comprehensive review. *Nano Energy* **2017**, *37*, 136–157.

(54) Stamenkovic, V. R.; Fowler, B.; Mun, B. S.; Wang, G.; Ross, P. N.; Lucas, C. A.; Marković, N. M. Improved oxygen reduction activity on  $\text{Pt}_3\text{Ni}$  (111) via increased surface site availability. *Science* **2007**, *315*, 493–497.

(55) Xia, W.; Mahmood, A.; Liang, Z.; Zou, R.; Guo, S. Earth-abundant nanomaterials for oxygen reduction. *Angew. Chem., Int. Ed.* **2016**, *55*, 2650–2676.

(56) Chen, W.; Huang, J.; Wei, J.; Zhou, D.; Cai, J.; He, Z.-D.; Chen, Y.-X. Origins of high onset overpotential of oxygen reduction reaction at Pt-based electrocatalysts: A mini review. *Electrochem. Commun.* **2018**, *96*, 71–76.

(57) Zhao, Z.; Xiang, H.; Dai, F.-Z.; Peng, Z.; Zhou, Y.  $(\text{La}_{0.2}\text{Ce}_{0.2}\text{Nd}_{0.2}\text{Sm}_{0.2}\text{Eu}_{0.2})_2\text{Zr}_2\text{O}_7$ : A novel high-entropy ceramic with low thermal conductivity and sluggish grain growth rate. *J. Mater. Sci. Technol.* **2019**, *35*, 2647–2651.

(58) Vayer, F.; Decorse, C.; Berardan, D.; Dragoe, N. New entropy-stabilized oxide with pyrochlore structure:  $\text{Dy}_2(\text{Ti}_{0.2}\text{Zr}_{0.2}\text{Hf}_{0.2}\text{Ge}_{0.2}\text{Sn}_{0.2})_2\text{O}_7$ . *J. Alloys Compd.* **2021**, *883*, 160773.

(59) Li, C.; Meng, B.; Fan, S.; Ping, X.; Fang, C.; Lin, W.; Chen, Y.; Zhang, H. Rare-earth-tantalate high-entropy ceramics with sluggish grain growth and low thermal conductivity. *Ceram. Int.* **2022**, *48*, 11124–11133.

(60) Retuerto, M.; Calle-Vallejo, F.; Pascual, L.; Lumbeeck, G.; Fernandez-Diaz, M. T.; Croft, M.; Gopalakrishnan, J.; Pena, M. A.; Hadermann, J.; Greenblatt, M.; et al.  $\text{La}_{1.5}\text{Sr}_{0.5}\text{NiMn}_{0.5}\text{Ru}_{0.5}\text{O}_6$  double perovskite with enhanced ORR/OER bifunctional catalytic activity. *ACS Appl. Mater. Interfaces* **2019**, *11*, 21454–21464.

(61) Kim, J. S.; Kim, B.; Kim, H.; Kang, K. Recent progress on multimetal oxide catalysts for the oxygen evolution reaction. *Adv. Energy Mater.* **2018**, *8*, 1702774.

(62) Wang, X.; Metz, P.; Cali, E.; Jothi, P. R.; Lass, E. A.; Page, K. Phase Selectivity and Stability in Compositionally Complex Nano  $(n\text{A}_{1/n})\text{Co}_2\text{O}_4$ . *Chem. Mater.* **2023**, *35*, 7283–7291.

(63) Coelho, A. A. TOPAS and TOPAS-Academic: an optimization program integrating computer algebra and crystallographic objects written in C++. *J. Appl. Crystallogr.* **2018**, *51*, 210–218.

(64) Chen, J.; Li, H.; Pei, Z.; Huang, Q.; Yuan, Z.; Wang, C.; Liao, X.; Henkelman, G.; Chen, Y.; Wei, L. Catalytic activity atlas of ternary Co–Fe–V metal oxides for the oxygen evolution reaction. *J. Mater. Chem. A* **2020**, *8*, 15951–15961.

(65) Singh, H.; Liyanage, W. P.; Nath, M. Carbon nanotube encapsulated metal selenide nanostructures for efficient electrocatalytic oxygen evolution reaction. *Chem. Commun.* **2022**, *58*, 8360–8363.

(66) Singh, H.; Marley-Hines, M.; Chakravarty, S.; Nath, M. Multi-walled carbon nanotube supported manganese selenide as a highly active bifunctional OER and ORR electrocatalyst. *J. Mater. Chem. A* **2022**, *10*, 6772–6784.

(67) Nath, M.; De Silva, U.; Singh, H.; Perkins, M.; Liyanage, W. P.; Umapathi, S.; Chakravarty, S.; Masud, J. Cobalt telluride: a highly efficient trifunctional electrocatalyst for water splitting and oxygen reduction. *ACS Appl. Energy Mater.* **2021**, *4*, 8158–8174.

(68) Lu, Y.; Deng, Y.; Lu, S.; Liu, Y.; Lang, J.; Cao, X.; Gu, H. MOF-derived cobalt–nickel phosphide nanoboxes as electrocatalysts for the hydrogen evolution reaction. *Nanoscale* **2019**, *11*, 21259–21265.

(69) Sajeev, A.; Paul, A. M.; Nivetha, R.; Gothandapani, K.; Gopal, T. S.; Jacob, G.; Muthuramamoorthy, M.; Pandiaraj, S.; Alodhayb, A.; Kim, S. Y.; et al. Development of Cu<sub>3</sub>N electrocatalyst for hydrogen evolution reaction in alkaline medium. *Sci. Rep.* **2022**, *12*, 2004.

(70) Zhuang, J.; Lu, B.; Gu, F.; Zhong, Z.; Su, F. Ordered mesoporous Cu–Ca–Zr: A superior catalyst for direct synthesis of methyl formate from syngas. *Carbon Resour. Convers.* **2018**, *1*, 174–182.

(71) Wang, X.; Zuo, Y.; Horta, S.; He, R.; Yang, L.; Ostovari Moghaddam, A.; Ibáñez, M.; Qi, X.; Cabot, A. CoFeNiMnZnB as a High-Entropy Metal Boride to Boost the Oxygen Evolution Reaction. *ACS Appl. Mater. Interfaces* **2022**, *14*, 48212–48219.

(72) Harada, M.; Kotegawa, F.; Kuwa, M. Structural changes of spinel  $\text{MCo}_2\text{O}_4$  (M = Mn, Fe, Co, Ni, and Zn) electrocatalysts during the oxygen evolution reaction investigated by in situ X-ray absorption spectroscopy. *ACS Appl. Energy Mater.* **2022**, *5*, 278–294.